CHARACTERIZATION OF HIGH T_c MATERIALS AND DEVICES BY ELECTRON MICROSCOPY

Edited by

NIGEL D. BROWNING
University of Illinois at Chicago

STEPHEN J. PENNYCOOK
Oak Ridge National Laboratory, Tennessee

CAMBRIDGE
UNIVERSITY PRESS

PUBLISHED BY THE PRESS SYNDICATE OF THE UNIVERSITY OF CAMBRIDGE
The Pitt Building, Trumpington Street, Cambridge, United Kingdom

CAMBRIDGE UNIVERSITY PRESS
The Edinburgh Building, Cambridge CB2 2RU, UK http://www.cup.cam.ac.uk
40 West 20th Street, New York, NY 10011-4211, USA http://www.cup.org
10 Stamford Road, Oakleigh, Melbourne 3166, Australia
Ruiz do Alarcón 13, 28014 Madrid, Spain

First published 2000

Printed in the United Kingdom at the University Press, Cambridge

Typeset in 11/14pt Times New Roman [KT]

A catalogue record for this book is available from the British Library

Library of Congress Cataloguing in Publication data
Characterization of high Tc materials and devices by electron
microscopy / edited by Nigel D. Browning, Stephen J. Pennycook.
p. cm.
ISBN 0 521 55490 X (hb)
1. High temperature superconductors. 2. Electron microscopy–Technique. I. Browning, Nigel D. II. Pennycook, Stephen J.
QC611.98.H54C43 1999
537.6′23′0284–dc21 99-18754 CIP

ISBN 0 521 55490 X hardback

Contents

1

High-resolution transmission electron microscopy

S. HORIUCHI and L. HE

1.1 Introduction

High-resolution transmission electron microscopy (HRTEM) has been widely and effectively used for analyzing crystal structures and lattice imperfections in various kinds of advanced materials on an atomic scale. This is especially the case for high T_c superconductors (HTSCs). The most characteristic feature in crystal structures of HTSCs is that there is a common structural element, a CuO_2 plane, in which superconductive carriers (positive holes or electrons) are transported. The remaining part, sandwiching the CuO_2 planes, accommodates additional oxygen atoms or lattice defects to provide carriers to the CuO_2 planes. This is known as the charge reservoir. The transition temperature between superconductive and non-superconductive states, T_c, strongly depends on the concentration of carriers in CuO_2 planes and the number of CuO_2 planes. Any charge reservoir is composed of some structural elements, including lattice defects. An aim of HRTEM is to clarify the structure of the charge reservoirs. Additionally, a variety of microstructures strongly affect the critical current density, J_c, since they closely relate to the weak link at boundaries between superconductive grains as well as to the pinning of magnetic fluxoids. The characterization of point defects, dislocations, stacking faults, precipitates, grain boundaries, interfaces and surface structures is another important aim of HRTEM. In this chapter, we describe some fundamental issues in analyzing crystal structures and microstructures in HTSCs by HRTEM.

1.2 Theoretical background for HRTEM

HRTEM images closely depend not only on some optical factors in the imaging process by the electron lens, but also on a scattering process of the electrons

incident on the crystal specimen [1.1]. This section describes the electron-optical background for HRTEM.

1.2.1 Phase contrast

Let us begin with a simple case where a central beam and one diffracted beam pass through the objective aperture of an electron microscope. Both beams starting from a site in the bottom surface of a thin specimen meet again at the image plane to form an image. With their contributions at the site x_i on the image plane, $\Psi_o(x_i)$ and $\Psi_g(x_i)$, the amplitude and intensity of the resultant wave, $\Psi(x_i)$ and $I(x_i)$, can be expressed as

$$\begin{aligned} \Psi(x_i) &= \Psi_o(x_i) + \Psi_g(x_i) \\ I(x_i) &= \Psi(x_i)\Psi^*(x_i) \\ &= I_o(x_i) + I_g(x_i) + 2\mathrm{Re}[\Psi_o(x_i)\Psi_g^*(x_i)], \end{aligned} \tag{1.1}$$

where $I_o(x_i) = |\Psi_o(x_i)|^2$ and $I_g(x_i) = |\Psi_g(x_i)|^2$. Re means that only the real part in the bracket should be considered. Here it is assumed that both waves can interfere coherently.

A phase difference arises between $\Psi_o(x_i)$ and $\Psi_g(x_i)$ mainly because of the difference in the path length. As a result, interference fringes (a lattice image) appear in the image. The image contrast is called phase contrast since it owes its origin to the phase difference. For a very thin specimen with an incident beam of unit amplitude, $I_0 = 1 \gg I_g$,

$$I(x_i) = 1 + 2\,\mathrm{Re}[\Psi_g^*(x_i)], \tag{1.2}$$

where the magnification is assumed to be 1. The image contrast is proportional to the diffraction amplitude. This means that appreciable contrast can be obtained even from very small subjects like a single atom, a fine particle or a thin film, whose scattering power is very small. For comparison, the so-called diffraction contrast, another image contrast mechanism widely used for characterizing large scale defects like dislocations, is proportional to the diffracted intensity.

1.2.2 Lattice image and structure image

Let us consider the imaging mechanism of a lattice image using Fig. 1.1(a) [1.1]. First, diffraction waves are excited by a substance. After passing through the electron lens the diffraction pattern is formed on the back focal plane. The intensity maximum of each reflection is designated as 0, $\pm 1, \ldots, \pm h, \ldots$. Secondly, these spots become new sources so that the electrons starting here

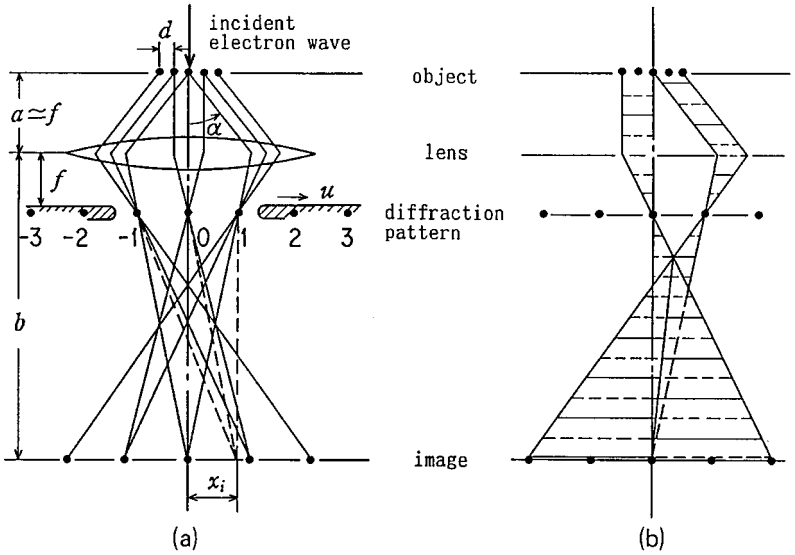

Fig. 1.1. (a) Optical geometry for HRTEM; (b) phase of the central and scattered waves under the imaging conditions for forming a crystal structure image. The phase difference of these two waves becomes π at the sites of atoms in the image plane.

meet again at the image plane to form a lattice image. Since the distance between the back focal plane and the image plane ($= b–f$) is actually very large as compared to the extension of the diffraction spots, the interference pattern on the image plane can be taken to be due to Fraunhofer diffraction. The amplitude of a lattice image $\Psi(x_i)$ is then described by

$$\Psi(x_i) = \mathscr{F}[Q(h)A(h)\exp\{2\pi i\chi(h)\}], \tag{1.3}$$

where Q is the amplitude of diffracted waves at site h, A the effect of the objective aperture, and $2\pi\chi$ the amount of phase change on passing through the electron lens. $\mathscr{F}$ denotes Fourier transformation.

In one of the through-focal series of lattice images, which are taken using many diffracted beams, the sites of dark spots coincide with those of atom columns parallel to the incident electron beam. This image is called the crystal structure image or simply structure image. Examples of structure images will be shown later (cf. Figs. 1.4, 1.8 and 1.11). In a structure image, the arrangement of dark spots corresponds to that of atom columns uniquely. In many cases, we can read out only the sites of heavy atoms. However, if we can speculate on the sites of all the atoms, including the light atoms, with help from crystal symmetry and crystal chemistry, we may call this a structure image as well.

1.2.3 Phase contrast transfer function

Electrons change the phase on passing through an electron lens due to the spherical aberration and defocus. The aberration function $\chi(u)$, proportional to the change in phase of the electron wave, is described by

$$\chi = \varepsilon\lambda u^2/2 - C_s\lambda^3 u^4/4, \tag{1.4}$$

where ε is the amount of defocus, λ the wavelength of electrons, u the spatial frequency and C_s the spherical aberration constant [1.2].

The phase factor $\exp\{2\pi i\chi(u)\}$ in eq. (1.3) strongly affects the intensity of lattice images. The function $\sin(2\pi\chi)$ is very important to determine, and is called the phase contrast transfer function. Fig. 1.2 shows some calculated results of the function with parameters, E (accelerating voltage) = 200 kV and $C_s = 1.2$ mm, for the range between $\varepsilon = 900$ and -500 Å [1.1]. The horizontal axis is scaled by the value of u ($= 1/d$ where d is the interplanar spacing). The value of the function fluctuates between 1 and -1. The fluctuation is more prominent at higher ranges of u. It is noted that $\sin(2\pi\chi) = 1$ in the range between $u = 1/2.5$ and $1/6$ Å^{-1} at $\varepsilon = 650$ Å.

1.2.4 Weak phase object approximation

Electrons entering into any material are affected by the electrostatic potential field V and, as a result, change their phase. For electrons running in the z direction, the phase change is described by

$$q(r_0) = \exp\left(i\sigma\int V\,\mathrm{d}z\right), \tag{1.5}$$

where σ is the interaction parameter. q is called the transmission function. When the crystal is so thin that the relation

$$\sigma\int V\,\mathrm{d}z(=\sigma V_p) \ll 1 \tag{1.6}$$

holds, eq. (1.5) can be expanded as follows:

$$q(r_0) = 1 + i\sigma V_p(r_0), \tag{1.7}$$

where V_p is the projected potential of crystal, $r_0 = (x_0, y_0)$ the two-dimensional positional vector in the objective plane. This is the approximation of a weak phase object. Since i represents the phase change of $\pi/2$, eq. (1.7) means the sum of the central beam with amplitude 1 and the scattered electron waves with amplitude $i\sigma V_p(r_0)$.

On the Fourier transformation of eq. (1.7) we get

$$\mathscr{F}[q(r_0)] = Q(u) = \delta(u) + i\sigma\mathscr{F}[V_p(r_0)] \tag{1.8}$$

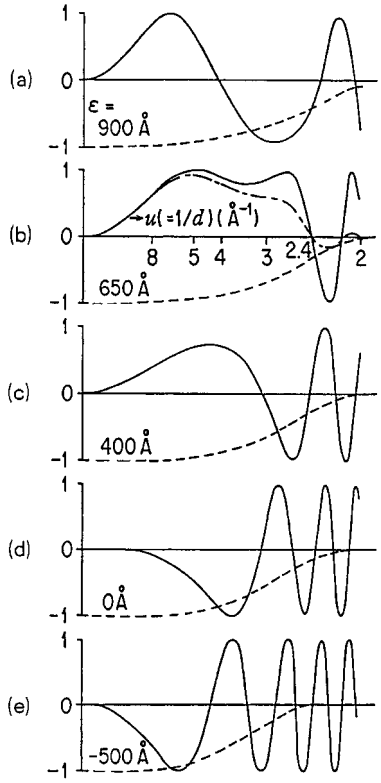

Fig. 1.2. Phase contrast transfer function $\sin(2\pi\chi)$ (solid line) and attenuation function $-E_D E_j$ (broken line) against u, for $E = 200$ kV and $C_s = 1.2$ mm.

where $\delta(u)$ is the delta function. The Fourier transform of the second term has the following value

$$\mathscr{F}[V_p(r_0)] = V_u \Delta z = (48.0/\Omega) F(u) \Delta z, \tag{1.9}$$

where V_u is the Fourier coefficient of potential, Ω the volume of unit-cell and $F(u)$ the crystal structure factor, the atomic structure factor f_j summed over sites j,

$$F(u) = F_{hk0} + \sum_j f_j \exp[-2\pi i\{h(x_{0j}/a) + k(y_{0j}/b)\}]. \tag{1.10}$$

1.2.5 Scherzer imaging condition

On substituting eqs. (1.8) and (1.9) into eq. (1.3) we get

$$\Psi(r_i) = \mathscr{F}[\{\delta(u) + i\sigma V_u \Delta z\}\{\cos 2\pi\chi(u) + i \sin 2\pi\chi(u)\}]$$
$$= 1 - \sigma \Delta z \mathscr{F}[V_u\{\sin 2\pi\chi(u) - i \cos 2\pi\chi(u)\}] \quad (1.11)$$

where the size of objective aperture is assumed to be infinite. The image intensity is

$$I(r_i) = 1 - 2\sigma \Delta z \mathscr{F}[V_u\{\sin 2\pi\chi(u)]. \quad (1.12)$$

We note from this formula that the image contrast closely depends on the phase contrast transfer function $\sin 2\pi\chi(u)$. As shown in Fig. 1.2, the value of $\sin 2\pi\chi(u)$ changes strongly depending on the defocus ε. However, if such a condition as

$$\sin 2\pi\chi(u) = 1 \quad (1.13)$$

holds, the image intensity will be [1.3]

$$I(r_i) = 1 - 2\sigma V_p(r_0). \quad (1.14)$$

Therefore, we can expect that the projected potential $V_p(r_0)$ is reflected in the image; the site with large value of V_p shows a dark contrast, while that with low V_p shows a bright one. This is a general principle for the formation of the structure image; sites of heavy metal atoms having high potential are imaged as dark dots. In order to realize the relation of eq. (1.13) as widely as possible we assume

$$2\pi\chi_{max} = 0.7\pi$$
$$\therefore \sin 2\pi\chi_{max} = 0.81.$$

The defocus value corresponding to this, ε_s, is

$$\varepsilon_s = 1.2 C_s^{1/2} \lambda^{1/2}. \quad (1.15a)$$

At this defocus the value of spatial frequency, u_s, for which the value of χ first becomes zero, is

$$u_s = 1.5 C_s^{-1/4} \lambda^{-3/4}. \quad (1.15b)$$

Therefore, a structure image can be obtained from a weak phase object first by setting the defocus value at ε_s and then by cutting out those diffracted waves whose spatial frequencies are larger than u_s. These observation conditions derived from eq. (1.13) are called the Scherzer imaging conditions and the defocus value ε_s is called the Scherzer focus.

Let us consider the phase change at the Scherzer focus geometrically. In Fig. 1.1(b) solid and broken lines represent the peaks and valleys of the phase, respectively, for the central and diffracted waves [1.1]. For simplicity, only one

diffracted wave is shown. The phase of the diffracted wave is advanced first by $\pi/2$ on scattering and secondly also by $\pi/2$ on passing through an electron lens (since $\sin 2\pi\chi(u) = 1$). As a result, the phase difference between the central wave and the diffracted wave becomes π. On the image plane, therefore, destructive interference occurs between them to cause the atom sites to appear dark.

1.2.6 Resolution limit for HRTEM

The maximum scattering angle under the Scherzer condition, $\alpha_{\max}$, and the corresponding lattice spacing, d_s, are

$$\alpha_{\max} = \lambda u_s = 1.5 C_s^{-1/4} \lambda^{1/4} \tag{1.16a}$$

$$d_s = 1/u_s = 0.65 C_s^{1/4} \lambda^{3/4} \tag{1.16b}$$

d_s is the minimum spacing in the information contributing to imaging and is called the resolution limit due to spherical aberration, or the Scherzer resolution limit. It is essentially the resolving power of HRTEM. We note from this that C_s and λ must be made smaller to obtain a higher resolving power.

1.2.7 Extension of weak phase object approximation

The weak phase object approximation (eq. (1.6)) is satisfied when $V_p(= V_0 \Delta z) \ll 1.2 \times 10^3$ VÅ for $E = 200$ kV. This means $\Delta z \ll 120 \sim 40$ Å since V_0 (mean inner potential) $= 10 \sim 30$ V for most inorganic crystals. In reality, however, structure images are obtained mostly for thickness between 15 and 50 Å, depending on the material, crystal structure and orientation, and accelerating voltage. That is to say, the condition for the weak phase object is not satisfied in most actual cases.

In order to overcome this contradiction we extend the theory of weak phase object approximation to slightly thicker crystals as follows; from dynamical calculations on the amplitude and phase of many waves we note the existence of such a relation as

$$Q(u) = Q'(u) \exp(iB\Delta z) \tag{1.17}$$

where B is constant for each of the scattered waves and 0 for the central wave as long as the crystal thickness is less than that for the first extinction. Besides, the amplitude of the scattered waves is still considerably less than that of the central wave, and the relative intensities of the scattered waves are almost the same as for kinematical scattering [1.4]. It is therefore reasonable to assume that $\mathscr{F}[Q'(u)]$ essentially resembles $\exp(i\sigma V_p)$. Then we obtain

$$\Psi(r_i) \propto \exp\{i\sigma V_p(r_0)\} * \mathscr{F}[\exp\{2\pi i(\chi + B\Delta z)\}] \tag{1.18}$$

where $*$ means the convolution integral and the size of the objective aperture is assumed to be infinite. A similar formula can be derived from wave mechanical considerations [1.1]. Eq. (1.18) means that we have only to consider the effect of the total phase change. The wave aberration $2\pi\chi$ and the phase change $2\pi B\Delta z$ due to the dynamical effect of electron diffraction are therefore equivalent from the viewpoint of the transfer of phase contrast. The Scherzer imaging condition (eq. (1.13)) should then be modified to

$$\sin\{2\pi(\chi + B\Delta z)\} = 1. \tag{1.19}$$

In fact, the optimum focus at which the structure image is obtained is in most cases not at the Scherzer focus ε_s (eq. (15a)) but slightly shifted towards the Gaussian focus, depending on thickness. This is due to the effect of the phase shift by the dynamical scattering. According to a numerical calculation, for example [1.1], the main part of the modified transfer function already deviates from the condition of $\sin 2\pi\chi = 1$ at a thickness of only 16 Å for a crystal with heavy elements such as $2Nb_2O_5 \cdot 7WO_3$, and the optimum defocus shifts from 1000 to 500 Å for a thickness near 50 Å.

1.2.8 Effect of the coherence among electron waves

On the formation of lattice images the amplitudes of waves are integrated. This means that we must consider the interference among them under coherent conditions. In fact, the chromatic aberration and the beam convergence effects seriously deteriorate the coherence and, as a result, the image intensity is decreased. The degree of coherence among electron waves can be described by a function which is called the transmission cross coefficient. Using this function we can estimate the effect of the coherence degradation for the weak phase object as follows

$$I(r_i) = 1 - 2\sigma\Delta z\mathscr{F}[V_u \sin\{2\pi\chi(u)\} E_D(u, \varepsilon) E_j(u, \varepsilon)] \tag{1.20a}$$

$$E_D(u, \varepsilon) = \exp(-0.5\pi^2\lambda^2\Delta^2 u^4) \tag{1.20b}$$

$$E_j(u, \varepsilon) = \exp\{-(\pi u_0)^2[(\varepsilon - C_s\lambda^2 u^2)\lambda u]^2\} \tag{1.20c}$$

where Δ is the mean fluctuation of focus due to the chromatic aberration and u_0 the effective size of the electron source ($u_0 = \beta/\lambda$, where β is the semi-angle of the illumination convergence). On comparing with eq. (1.12) we note that the phase contrast transfer function $\sin\{2\pi\chi(u)\}$ is attenuated by the modulation function $E_j(u, \varepsilon)E_D(u, \varepsilon)$. In Fig. 1.2 the values of $-E_jE_D$ are plotted by broken lines. An example of the effective transfer function, obtained by the product between this and $\sin\{2\pi\chi(u)\}$, is shown by a chain line in Fig.

1.2(b). In the region of large spatial frequency the attenuation of the transfer function is prominent.

1.3 Techniques relevant to HRTEM

1.3.1 Electron-optical conditions to obtain an HRTEM image

Many-beam lattice images are usually obtained under the following electron-optical conditions. (1) The illuminating electron beam is axial. (2) It is incident along a low-order zone axis of the crystal. (3) The objective aperture has the size given by eq. (1.15b) or (1.16). (4) The specimen crystal is very thin. (5) The image is observed at the defocus given by eq. (1.15a), or, it is slightly shifted toward the Gaussian focus, depending on the thickness, as mentioned in relation to eq. (1.19).

A structure image appears in a through-focal series of many-beam lattice images. For getting a structure image, the specimen thickness must be thinner than a few tens of ångströms. Except for the case when a specimen is originally prepared as a thin film, this is achieved only by crushing a bulk material. The crushing method is applicable to crystals which break into fragments by cleavage.

On the other hand, for the observation of cross-sections of materials, for example prepared by CVD methods, specimens must be thinned by an ion-milling method. The resulting thickness is generally more than 100 Å. This means an optical artifact inevitably arises in the image, i.e. the correspondence between the image contrast and the crystal structure is no longer unique. The interpretation of such an image must be done even more carefully, using computer simulations of image intensities.

1.3.2 Procedure for observing an HRTEM image

A practical procedure for observing a many-beam lattice image is as follows. For simplicity, we assume a specimen fragment in the form of a sharp wedge is used, which has been prepared by the crushing method and supported on a carbon microgrid. (1) The specimen is observed with a magnification of about 1×10^4 times to look for an area which is very thin, clean and not distorted, at the edge of a fragment. (2) The orientation of a small crystal area is examined by means of a diffraction pattern. When Laue zones are found suggesting that the orientation is near to that intended, the tilting stage is operated so that the zone axis becomes parallel to the optical axis. (3) An objective aperture is inserted at the center of the diffraction pattern. (4) After confirmation of

voltage center, astigmatism is corrected by use of a stigmator. This is done by observing the granular structure of a microgrid film enlarged on a TV screen. (5) On changing slowly the amount of defocus, photographs are taken when the images anticipated in advance by means of the computer simulation of image intensity appear. For an unknown structure an image with high contrast appearing nearly at the Scherzer focus is recorded, and then several images are taken changing the defocus value for each in the direction to the Gaussian focus (a through-focal series of images). (6) A diffraction pattern is recorded to check how far the orientation has deviated from the zone axis during this procedure.

1.3.3 Computer simulation of an HRTEM image

Whether a structure model of a crystal or a defect obtained from an HRTEM image is correct or not must be examined. The method most widely practiced at present is to compare experimental images to calculated images obtained by computer simulation based on the structure model. The image intensity can be computed using commercially available or home-made software [1.1]. The calculation consists of two stages, i.e. the scattering stage and the imaging stage. In the former, dynamical diffraction amplitudes are computed usually by the multi-slice method [1.5]. During the course of this stage the projected potential of the crystal is also calculated.

1.3.4 Use of information from electron diffraction

Electron diffraction patterns include a great deal of information on crystal structure. They give valuable information that is complementary to that obtained from HTREM images, because they give more average and statistically significant information than images. For an example, lattice parameters are obtained more precisely from diffraction patterns than from images. Another example is the crystal symmetry and the related space group, which is derived from the extinctions of diffraction spots [1.1]. These are demonstrated by some concrete examples later.

1.4 HRTEM analysis of high T_c superconductors

In this section, some recent results on the structure analysis of HTSCs are shown in order to demonstrate the usefulness of HRTEM. In all cases mentioned here small blocks of specimens were lightly crushed in an agate mortar and the fragments obtained were observed in a high-resolution, high-voltage

electron microscope (model H-1500) at an accelerating voltage of 800 kV. The point-to-point resolving power has been measured to be 1.4 Å.

1.4.1 Structure analysis of $Ga_2(Sr, Nd)_4Nd_3Cu_4O_z$

Powders of Ga_2O_3, PbO, $SrCO_3$, Nd_2O_3 and CuO were mixed with a nominal composition of $(Ga_{1.78}Cu_{0.22})(Sr_{3.16}Nd_{0.84})Nd_3Cu_4O_{16-y}$. The mixture was heated in air at 1000 °C for 20 h with intermediate grindings. It was then heated at 1070 °C for 2 h under the oxygen pressure of 20 MPa, using a hot isostatic pressing (HIP) apparatus [1.6]. According to a powder X-ray diffraction the unit cell of the product crystal is $a = 5.458$, $b = 5.535$ and $c = 51.302$ Å (orthorhombic). Using energy dispersive X-ray spectroscopy (EDS) the composition of the product was measured to be $(Ga_{1.8}Cu_{0.2})(Sr_3Nd)Nd_3Cu_4O_z$. We call this compound Ga-2434 hereafter for simplicity. Although it did not show any d.c. susceptibility, we have analyzed the crystal structure by HRTEM, since it appeared to be a new type of structure with interesting possibilities for superconductivity.

Electron diffraction patterns were taken from many crystal fragments of Ga-2434. Some typical patterns are shown in Fig. 1.3. From the reflection conditions ($h + k = 2n$ for $hk0$, $l = 2n$ for $0kl$, $h0l$ and $00l$, $h = 2n$ for $h00$ and $k = 2n$ for $0k0$) the space group is uniquely determined to be *Pccn* (56). The lattice parameters are $a = 5.46$, $b = 5.54$ and $c = 51.3$ Å, being in agreement with those obtained from X-ray diffraction. Weak diffuse streaks along [010] in Fig. 1.3(a) must be due to stacking faults, which have been observed locally as intergrowth defects.

Fig. 1.4 is an HRTEM image corresponding to the diffraction pattern in Fig. 1.3(c), in which the electron beam is incident along the [110] direction. We see two adjoining lines and a single line of the darkest spots, as marked by large and small, leftward arrows, respectively. The image was taken near to Scherzer focus (the calculated Scherzer focus ε_s is 570 Å underfocus, while the real defocus is about 450 Å underfocus) so that the darker spots mark the sites of the heavier atom columns. Therefore, we may correlate the darkest spots to Nd atom columns, the second darkest spots to Sr columns and the least dark ones to Ga or Cu atoms. As a result, we can depict the structure of the present crystal like that in Fig. 1.5, i.e. the crystal is composed of a stacking of different atomic sheets, having the sequence $GaO/SrO^{*1}/CuO_2/(NdO)_2/CuO_2/SrO^{*1}/GaO/SrO^{*2}/CuO_2/Nd/CuO_2/SrO^{*2}/GaO$.

When we examine the image contrast of Fig. 1.4 in more detail, we note that there are two kinds of darkness for the SrO planes, i.e. the atom column sites of SrO^{*1} plane, marked by arrow 1, are slightly darker than those of the SrO^{*2}

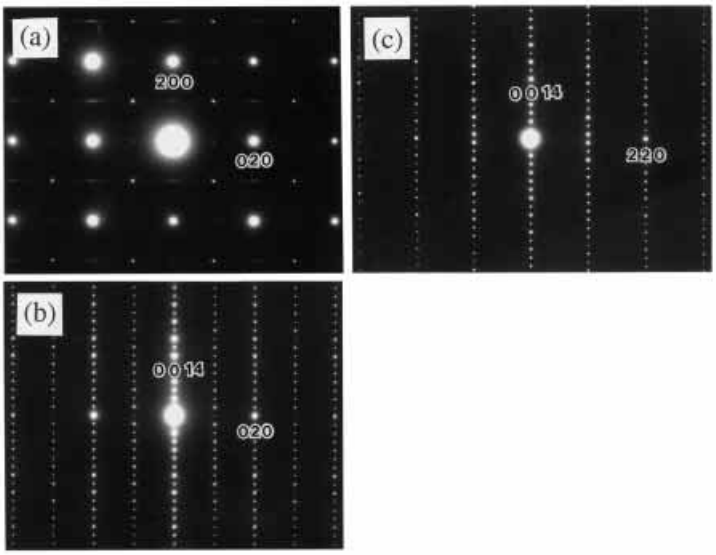

Fig. 1.3. Electron diffraction patterns taken from a Ga-2434 crystal. The electron beam is incident along [001] (a), [100] (b) and [110] (c). From the reflection conditions the space group of the crystal is determined to be *Pccn*.

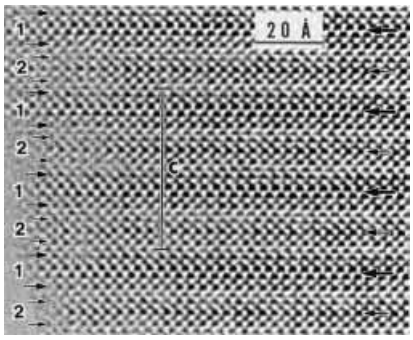

Fig. 1.4. HRTEM image of Ga-2434 corresponding to the diffraction pattern of Fig. 1.3(c). The darkest spots on the lines marked by large and small leftward arrows indicate the columns of Nd atoms in $(NdO)_2$ and Nd planes, respectively. Rightward arrows 1 and 2 show the SrO^{*1} and SrO^{*2} planes in Fig. 1.5, respectively. $c = 51.3$ Å.

plane, marked by arrow 2. This suggests that the planes labeled 1 may include Nd atoms to some extent. In order to solve the problem, we have computed the image intensity on changing the occupational probability of Nd atoms in the SrO*[1] plane, which is now denoted by $(Sr_{1-x}Nd_x)O$. The computed images for $x = 0.3$, 0.5 and 0.7 are shown in Fig. 1.6. On comparing them to the real image of Fig. 1.4, the best fit is obtained for $x = 0.5$. The composition corresponding to $x = 0.5$ is identical with what is expected from the composition measured by EDX mentioned above. If the composition of $x > 0.5$ could be realized in an oxidizing atmosphere, the crystal could be superconducting, although this has not been the case so far.

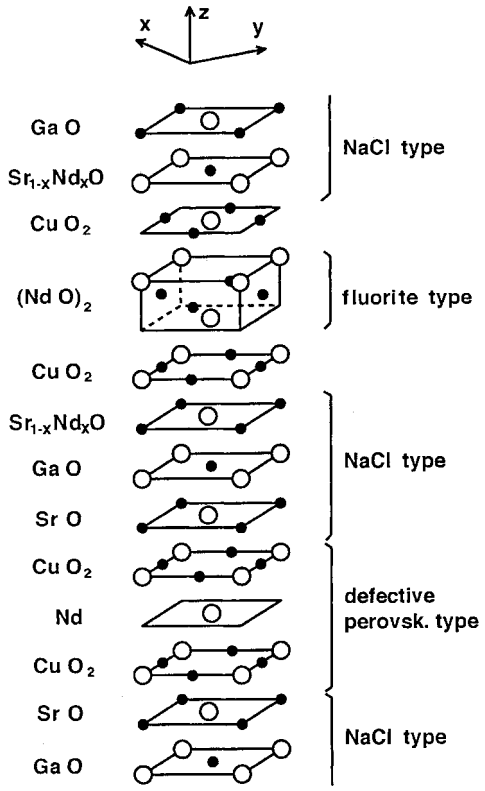

Fig. 1.5. Stacking sequence of atomic planes in a Ga-2434 crystal, constructed directly from an HRTEM image in Fig. 1.4. That corresponding to a half unit-cell length is shown ($c/2 = 25.65$ Å). Open circles stand for cations, closed ones for oxygens.

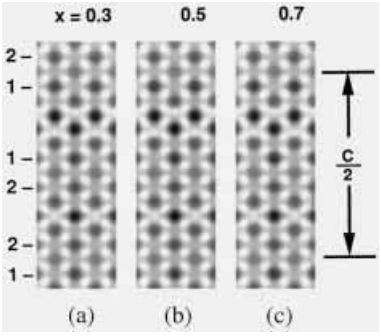

Fig. 1.6. Computer-simulated images of a Ga-2434 crystal, calculated for different occupational probabilities of Nd atoms in the SrO^{*1} plane, whose composition is denoted by $(Sr_{1-x}Nd_x)O$; $x = 0.3$ (a), $x = 0.5$ (b) and $x = 0.7$ (c). 1 and 2 indicate the SrO^{*1} and SrO^{*2} planes in Fig. 1.5, respectively.

1.4.2 Crystal structure and projected potential in $YBa_2Cu_4O_x$

Figure 1.7(a) shows a crystal structure of $YBa_2Cu_4O_x$ (124 phase, $a = 3.84$, $b = 3.87$ and $c = 27.24$ Å, orthorhombic). It contains the —Cu—O—Cu— single and double chains [1.7, 1.8] along [010], marked by S and D respectively. T_c of the 124 phase is known to be almost fixed (80 $\sim$ 82 K), since the range of variable oxygen content is very small. Fig. 1.8 is an HRTEM image of the 124 crystal, prepared under the pressure of 1.3 GPa [1.9]. The electron beam is incident along the [100] direction. Each site of cation columns is imaged as a dark spot. It is moreover noted that a Cu site in the double chains, which consists of a column of only Cu atoms, show slightly less darkness than another Cu site in the single chain which consists of a —Cu—O—Cu— column. This is due to the difference in the electrostatic potential at the two sites which can be checked by calculation. Fig. 1.7(b) shows the calculated image of the 124 phase. It is clear that the column sites of Cu atoms in the double chains show slightly less darkness than those of —Cu—O—Cu— in the single chain, in agreement with the observation. A computed projected potential (cf. eq. (1.6)) is shown in Fig. 1.7(c). It is clear that the projected potential of the column sites of Cu ions in the double chains is slightly lower than that of —Cu—O—Cu— ions in the single chain. This result indicates that the computer simulation of the projected potential is sometimes useful for the correct interpretation of the image contrast, in addition to simulation of the image intensity.

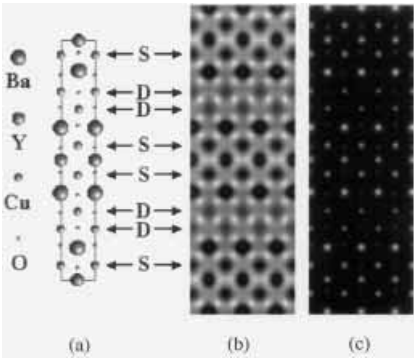

Fig. 1.7. (a) A structure model of $YBa_2Cu_4O_x$ (124 phase) projected along [100]. S and D mean the —Cu—O—Cu— single and double chains, respectively. (b) is the computer-simulated image and (c) the projected potential. For (b) $\varepsilon = 450$ Å (underfocus), $\Delta z = 30$ Å, $E = 800$ kV, $C_s = 2.2$ mm, $\Delta = 100$ Å and $\beta = 0.5$ mrad.

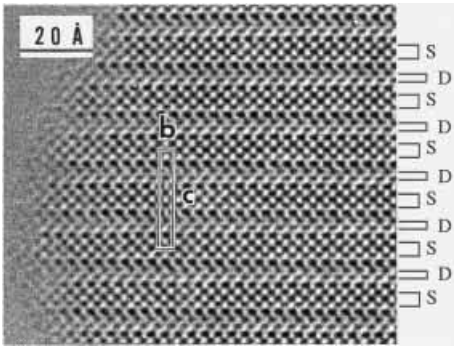

Fig. 1.8. HRTEM image of the 124 crystal taken with the incident beam along the [100] direction. The Cu column sites in the double chains (marked by D) show weak contrast as compared to —Cu—O—Cu— column sites in the single chain (S). $c = 27.24$ Å.

1.4.3 Visualization of oxygen atoms in $YBa_2Cu_3O_{+x}$

HRTEM would be more useful if all species of constituent atoms including light elements like oxygen could be visualized. This has become possible by a new ultra-high-resolution high-voltage electron microscope (UHR-HVEM, model H-1500) [1.10, 1.11]. Using the UHR-HVEM we have observed oxygen atoms

in high T_c superconductors, $YBa_2Cu_3O_{7.7}$ [1.12] and $YBa_2Cu_3O_{6.4}$ [1.13]. Here we clarify the conditions for observing oxygen atoms, with the help of a map showing the relationship between crystal thickness and defocus value.

It is known [1.14] that $YBa_2Cu_3O_{6+x}$ has an orthorhombic phase for $0.35 < x < 1$ (e.g. $a = 3.82$, $b = 3.89$ and $c = 11.68$ Å, for $x = 0.93$) and a tetragonal phase for $0 < x < 0.35$ (e.g. $a = b = 3.86$ and $c = 11.78$ Å, for $x = 0.34$). They are essentially similar to each other, i.e. the positions of the metal atoms are almost the same for both structures. The structure can simply be denoted by the stacking sequence of $BaO/CuO_2/Y/CuO_2/BaO/CuO_y$ planes. The total content $6 + x$ depends on how many oxygens exist in the CuO_y planes. In the present calculation, a tetragonal structure model, as shown in Fig. 1.9(a), is used for simplicity. The metal atoms are in the positions mentioned above. Excess oxygens are assumed to occupy all possible sites in the CuO_y planes. In the actual process of calculation the structure was simplified; there are three subcells in the model of Fig. 1.9(a). They are averaged so that a simplified unit-cell as shown in Fig. 1.9(b) can be assumed. The unit-cell is substantially the same as that for the perovskite-type structure. The site at the center (A site) is occupied by $(2/3)Ba + (1/3)Y$, sites at the corners by Cu, and sites at the edge centers by oxygen. The sites O1, O2 and O3 are fully occupied in the first stage of the calculation.

The image pattern and the image contrast strongly depend not only on the amount of defocus but also on the crystal thickness [1.15]. Figure 1.10 shows a defocus vs. thickness map for simulated images for [001] incidence. Some characteristic image patterns, which are apparently related to the real structure, appear in the definite areas outlined in the diagram. In an area marked by D1, column sites of Ba(Y) atoms are imaged as strong dark spots. Columns of —Cu—O—Cu— are imaged as medium dark spots. Columns containing only oxygen atoms are imaged as weak dark spots. The defocus is near the Scherzer condition. Since the scattering power of the —Cu—O—Cu— column is determined mainly by the Cu, this column is hereafter referred to as a 'column of Cu'.

In area D2 an image with dark spots is also obtained. The sites of metal atom columns are imaged but those of oxygens are not. In areas D3 and D4 the oxygen column sites are seen dark and the metal atom columns are less dark. In areas B1 and B2, on the other hand, bright-spot images appear; the image patterns are similar to those mentioned above but the contrast is reversed. In the area B1, sites of both Ba(Y) and Cu columns are imaged as strong bright spots, while the oxygen columns are seen less bright. In B2, the sites of oxygen columns are the brightest, while those of metal atom columns are less bright. An arrow on the lateral axis shows the center position of the first thickness

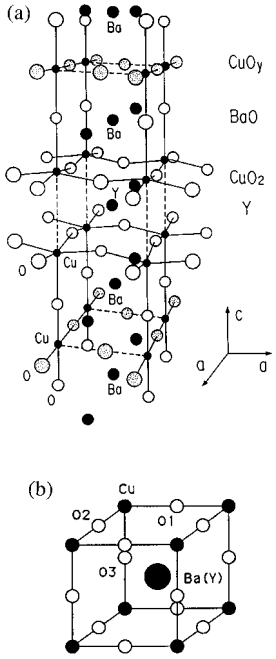

Fig. 1.9. (a) A structure model of $YBa_2Cu_3O_{8.0}$; (b) a simplified structure model for computer simulation. $a = 3.86$ Å and $c = 3.91$ Å (tetragonal).

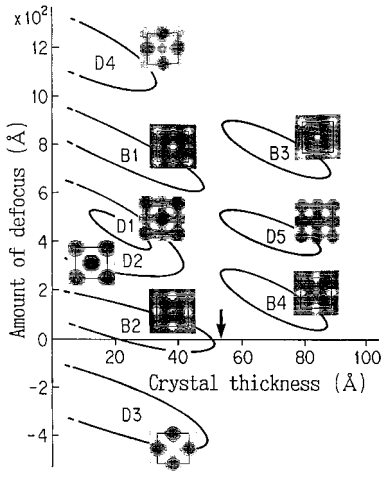

Fig. 1.10. Defocus vs. thickness map, showing computer simulated image contrast. D denotes a dark-spot image, B a bright-spot image. For each defocus value, images are calculated for crystal thicknesses of 23.5 Å and 74.3 Å, with $E = 800$ kV, $C_s = 2.2$ mm, $\Delta = 100$ Å and $\beta = 0.5$ mrad.

contour. In a crystal thicker than this there are also regions of bright- as well as dark-spot images; areas B3, B4 and D5, but no structure images are observed in these areas. In B4, for example, the oxygen column sites are very bright, while the metal atom columns are less bright. In Fig. 1.10 we note that each area extends in a downward direction with increasing thickness. This is because each of the scattered waves slowly increases its phase with increasing thickness due to their dynamical interaction [1.4], as mentioned in relation to eqs. (1.17)–(1.19).

A small sintered block of $YBa_2Cu_3O_{6.4}$ crystal ($T_c = 27$ K, orthorhombic, $a = 3.84$, $b = 3.87$ and $c = 11.73$ Å) [1.13] was lightly crushed, and the fragments obtained were observed in the UHR-HVEM. The accelerating voltage was selected at 800 kV in order to suppress the irradiation damage as far as possible [1.12, 1.13]. Figure 1.11 shows a through-focal series of images from a very thin part of the crystal, taken with incident electrons parallel to the [001] direction. The direct magnification was 3.5×10^5 times, and the exposure time was 2 s.

Figures 1.11(a), (b), (c), (d) and (e) are electron micrographs taken at a defocus of about 800 Å (underfocus), 450 Å, 300 Å, 50 Å and −300 Å (overfocus), respectively. Figures 1.11(a) and (d) are bright-spot images, while Figs. 1.11(b), (c) and (e) are dark-spot images. The image contrast is apparently reversed between (a) and (b), (c) and (d), and (d) and (e). Images calculated for the areas B1, D1, D2, B2 and D3 in Fig. 1.10 are inserted in Fig. 1.11 with the same magnification. It is noted that they almost fit to each other. In (b) small dark spots are clear at the sites of the arrowheads; the columns of oxygen atoms can clearly be discriminated beside those of the metal atoms.

It has been shown in a previous paper on ZrO_2 [1.15] that 'dark-spot images' correctly reflect the real structures of defects, while 'bright-spot images' do not. In order to confirm this also in the present case we have carried out further computer simulations of the image contrast. In the structure model of Fig. 1.9(a) all the oxygen atoms in the CuO_y planes were deleted; the total composition is then $YBa_2Cu_3O_{6.0}$. The occupational probability of the oxygen sites O1 and O2 in Fig. 1.9(b) becomes $2/3$. This means that the oxygen columns in the [001] projection of Fig. 1.12(a) have an occupational probability of $2/3$.

Figures 1.12(b) and (c) are the results of image calculations for the underfocus of $\varepsilon = 800$ and 450 Å, respectively. The crystal thickness is assumed to be 23.5 Å. For comparison, Figs. 1.12(d) and (e) show simulations using the same defocus values as the crystal with fully occupied oxygen columns. These are the values used for B1 and D1 in Fig. 1.10, respectively. The difference in the oxygen occupation is clearly visible in the contrast of the dark-spot images

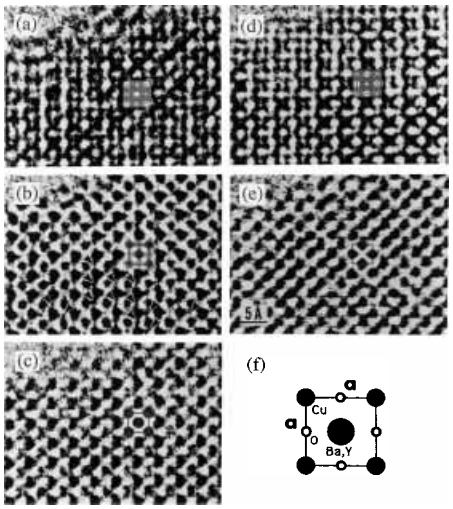

Fig. 1.11. Through-focal series of UHR-HVEM images for a very thin part of $YBa_2Cu_3O_{6.4}$, taken with the incident beam parallel to [001] at an accelerating voltage of 800 kV. The defocus value is 800 Å (underfocus) (a), 450 Å (b), 300 Å (c), 50 Å (d) and −300 Å (e). (f) is the projected structure of the unit-cell. At the sites arrowed in (b) small but clear dark spots are visible, showing the sites of oxygen atom columns.

(Figs. 1.12(c) and (e)). This is not the case in the bright-spot images ((b) and (d)); bright spots always appear at the oxygen column sites regardless of the oxygen occupation.

These results show that the fluctuation in intensity at the oxygen column sites of Fig. 1.11(b) is intuitively interpretable, while that of Fig. 1.11(a) is not; the dark spots of oxygen columns are clearly visible only at the sites marked by small arrows in Fig. 1.11(b). Similar investigations to these can be carried out for other regions in Fig. 1.10. In general, we conclude that the oxygen defects are visible and intuitively interpretable only in the area B1 of Fig. 1.10. The observation that the oxygen column sites become unclear near the edge of the fragment in Fig. 1.11(b) is because the contrast becomes very weak there. Local fluctuation of oxygen occupancy may be another possible reason.

Figure 1.13 shows the calculated image contrast vs. crystal thickness. The image contrast defined as $100 \times$ (background − peak intensity)/background, increases with increasing thickness, and at the thickness of about 25 Å, reaches about 80% for Ba(Y) columns and about 20% for oxygen columns.

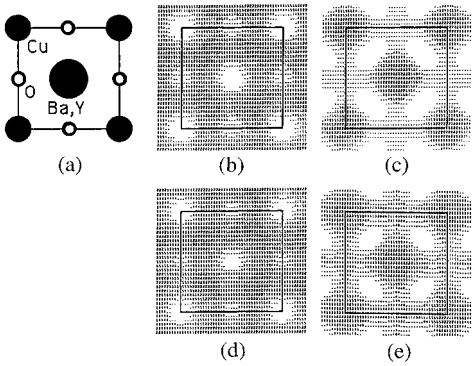

Fig. 1.12. Calculated images for $YBa_2Cu_3O_{8.0}$. (a) Projected structure in the [001] direction, $a = b = 3.86$ Å. (b) and (c) are computer simulated images of a crystal with oxygen defects at a thickness of 23.5 Å, with $\varepsilon = 800$ Å for (b) and $\varepsilon = 450$ Å for (c). (d) and (e) are calculated images for a defect-free crystal at a thickness of 23.5 Å, with $\varepsilon = 800$ Å and 450 Å, respectively.

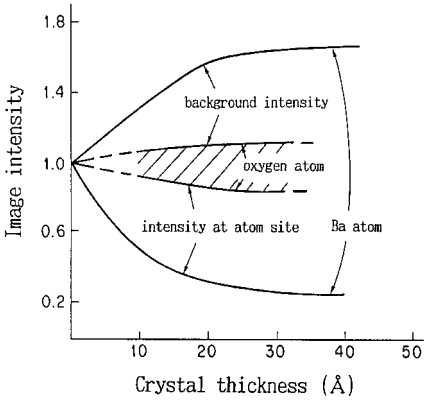

Fig. 1.13. The relationship between the image intensity and the thickness for Ba and oxygen columns in a $YBa_2Cu_3O_{8.0}$ crystal. The image contrast at Ba and oxygen columns sites are 80% and 20%, respectively, at a thickness of about 25 Å.

References

[1.1] S. Horiuchi, *Fundamentals of high-resolution transmission electron microscopy*, chs. 6–8 (North-Holland, 1994).
[1.2] O. Scherzer, *J. Appl. Phys.* **20**, 20 (1949).
[1.3] J. M. Cowley & S. Iijima, *Z. Naturforsch*. **27**, 445 (1972).

[1.4] S. Horiuchi, *Ultramicrosc.* **10**, 229 (1982).
[1.5] J. M. Cowley & A. F. Moodie, *Acta Crystallog. A* **30**, 280 (1974).
[1.6] A. Ono, L. L. Hu & S. Horiuchi, *Physica C* **247**, 91 (1995).
[1.7] J. Karpinski *et al.*, *Nature* **336**, 660 (1988).
[1.8] P. Marsh *et al.*, *Nature* **334**, 141 (1988).
[1.9] A. Ono & S.Horiuchi, *Physica C* **247**, 319 (1995).
[1.10] S. Horiuchi *et al.*, *Ultramicrosc.* **39**, 231 (1991).
[1.11] Y. Matsui *et al*., *Ultramicrosc.* **39**, 8 (1991).
[1.12] S. Horiuchi, Y. Matsui & B. Okai, *Jpn. J. Appl. Phys.* **31**, L59 (1992).
[1.13] S. Horiuchi, *Jpn. J. Appl. Phys.* **31**, L1335 (1992).
[1.14] J. D. Jorgensen *et al.*, *Phys. Rev. B* **41**, 1863 (1990).
[1.15] S. Horiuchi & Y. Matsui, *Jpn. J. Appl. Phys.* **31**, L283 (1992).